Third-harmonic generation microscopy with focus-engineered beams: a numerical study

Nicolas Olivier and Emmanuel Beaurepaire

Laboratoire d'optique et biosciences, Ecole Polytechnique, CNRS, F-91128 Palaiseau, France, and INSERM U696, Palaiseau, France

nicolas.olivier@polytechnique.edu, emmanuel.beaurepaire@polytechnique.edu

Abstract: We use a vector field model to analyze third-harmonic generation (THG) from model geometries (interfaces, slabs, periodic structures) illuminated by Hermite-Gaussian (HG) and Laguerre-Gaussian (LG) beams focused by a high NA lens. Calculations show that phase matching conditions are significantly affected by the tailoring of the field distribution near focus. In the case of an interface parallel to the optical axis illuminated by an odd HG mode, the emission patterns and signal level reflect the relative orientation of the interface and the focal field structure. In the case of slabs and periodic structures, the emission patterns reflect the interplay between focal field distribution (amplitude and phase) and sample structure. Forward-to-backward emission ratios using different beam shapes provide sub-wavelength information about sample spatial frequencies.

OCIS codes: (180.6900) Three-dimensional microscopy; (190.4160) Multiharmonic generation; (170.3880) Medical and biomedical imaging.

References and links

1. E. Yew and C. Sheppard, "Second harmonic generation microscopy with tightly focused linearly and radially polarized beams," Opt. Commun. **275**, 453-457 (2007).
2. K. Yoshiki, R. Kanamaru, M. Hashimoto, N. Hashimoto, and T. Araki , "Second-harmonic-generation microscope using eight-segment polarization-mode converter to observe three-dimensional molecular orientation," Opt. Lett. **32**, 1680-1682 (2007).
3. V. V. Krishnamachari and E. O. Potma, "Focus-engineered coherent anti-Stokes Raman scattering microscopy: a numerical investigation," J. Opt. Soc. Am. A **24**, 1138-1147 (2007).
4. V. V. Krishnamachari and E. O. Potma, "Imaging chemical interfaces perpendicular to the optical axis with focus-engineered coherent anti-Stokes Raman scattering microscopy," Chem. Phys. **341**, 81-88 (2007).
5. Y. Barad, H. Eisenberg, M. Horowitz, and Y. Silberberg, "Nonlinear scanning laser microscopy by third harmonic generation," Appl. Phys. Lett. **70**, 922-924 (1997).
6. M. Müller, J. Squier, K. R. Wilson, and G. J. Brakenhoff, "3D-microscopy of transparent objects using third-harmonic generation," J. Microsc. **191**, 266-274 (1998).
7. D. Débarre and E. Beaurepaire, "Quantitative characterization of biological liquids for third-harmonic generation microscopy," Biophys. J. **92**, 603-612 (2007).
8. D. Yelin, and Y. Silberberg, "Laser scanning third-harmonic generation microscopy in biology," Opt. Express **5** (1999).
9. D. Oron, D. Yelin, E. Tal, S. Raz, R. Fachima, and Y. Silberberg, "Depth-resolved structural imaging by third-harmonic generation microscopy," J. Struct. Biol. **147**, 3-11 (2004).
10. D. Débarre, W. Supatto, E. Farge, B. Moulia, M.-C. Schanne-Klein, and E. Beaurepaire, "Velocimetric third-harmonic generation microscopy: micrometer-scale quantification of morphogenetic movements in unstained embryos," Opt. Lett. **29**, 2881-2883 (2004).
11. C.-K. Sun, S.-W. Chu, S.-Y. Chen, T.-H. Tsai, T.-M. Liu, C.-Y. Lin, and H.-J. Tsai, "Higher harmonic generation microscopy for developmental biology," J. Struct. Biol. **147**, 19-30 (2004).

#98503 - $15.00 USD Received 8 Jul 2008; revised 21 Aug 2008; accepted 21 Aug 2008; published 3 Sep 2008

12. W. Supatto, D. Débarre, B. Moulia, E. Brouzés, J.-L. Martin, E. Farge, and E. Beaurepaire, "In vivo modulation of morphogenetic movements in Drosophila embryos with femtosecond laser pulses," Proc. Nat. Acad. Sci. USA **102**, 1047-1052 (2005).
13. D. Débarre, W. Supatto, A.-M. Pena, A. Fabre, T. Tordjmann, L. Combettes, M.-C. Schanne-Klein, and E. Beaurepaire, "Imaging lipid bodies in cells and tissues using third-harmonic generation microscopy," Nat. Methods **3**, 47-53 (2006).
14. D. Débarre, W. Supatto, and E. Beaurepaire, "Structure sensitivity in third-harmonic generation microscopy," Opt. Lett. **30**, 2134-2136 (2005).
15. J.-X. Cheng and X. S. Xie, "Green's function formulation for third harmonic generation microscopy," J. Opt. Soc. Am. B **19**, 1604-1610 (2002).
16. B. Richards and E. Wolf, "Electromagnetic diffraction in optical systems II. Structure of the image field in an aplanetic system.," Proc. Royal Soc. A **253**, 358-379 (1959).
17. L. Novotny and B. Hecht, Principles of nano-optics (Cambridge Univ Press, 2006).
18. Boyd, R. W. *Nonlinear optics*, 2nd edition, (Academic Press 2003).
19. H. Kogelnik, and T. Li, "Laser beams and resonators," Appl. Opt. **5**, 1550 (1966).
20. K. Youngworth and T. Brown, "Focusing of high numerical aperture cylindrical-vector beams," Opt. Express **7**, 77-87 (2000).
21. D. Débarre, N. Olivier, and E. Beaurepaire, "Signal epidetection in third-harmonic generation microscopy of turbid media," Opt. Express **15**, 8913-8924 (2007).
22. E. Y. S. Yew, and C. J. R. Sheppard, "Fractional Gouy phase," Opt. Lett. **33**, 1363-1365 (2008).
23. J. Mertz, and L. Moreaux, "Second-harmonic generation by focused excitation of inhomogeneously distributed scatterers," Opt. Commun. **196**, 325-330 (2001).
24. C. J. R. Sheppard, "High-aperture beams," J. Opt. Soc. Am. A **18**, 1579-1587 (2001).
25. S. Quabis, R. Dorn, M. Eberler, O. Glöckl, and G. Leuchs, "Focusing light to a tighter spot," Opt. Commun. **179**, 1-7 (2000).
26. S. Carrasco, B. E. A. Saleh, M. C. Teich, and J. T. Fourkas, "Second- and third-harmonic generation with vector Gaussian beams," J. Opt. Soc. Am. B **23**, 2134-2141 (2006).
27. S. S. Sherif, M. R. Foreman, and P. Török, "Eigenfunction expansion of the electric fields in the focal region of a high numerical aperture focusing system," Opt. Express **16**, 3397-3407 (2008).
28. M. R. Foreman, S. S. Sherif, P. R. T. Munro, and P. Török, "Inversion of the Debye-Wolf diffraction integral using an eigenfunction representation of the electric fields in the focal region," Opt. Express **16**, 4901-4917 (2008).

1. Introduction

Coherent nonlinear microscopies based on parametric processes such as coherent anti-Stokes Raman scattering (CARS), second-harmonic generation (SHG) or third-harmonic generation (THG) are receiving considerable attention. All these imaging modalities are compatible with two-photon excited fluorescence microscopy and provide different information on biological and non biological media with micrometer 3D resolution. A remarkable property of coherent nonlinear imaging techniques is that they are very sensitive to both the sub-micrometer sample structure and to the focal field structure. Indeed, the far field signal results from the coherent superposition in the detection plane of waves emitted at different locations near focus, and interference phenomena define the visibility of a particular distribution of scatterers.

Engineering the focal field structure is therefore a logical step in coherent nonlinear imaging. Intensity, phase and polarization may be modified by controlling the wavefront at the pupil of the objective, resulting in a modulation of phase-matching conditions and far-field emission patterns. This concept has been explored recently for SHG microscopy, where focused beams with strong axial components were used to enhance signal from fibers parallel to the optical axis [1, 2], and in CARS microscopy where focus engineering was used to highlight interfaces [3, 4].

In this article, we study the use of engineered beams in THG microscopy. THG microscopy relies on the third-order nonlinear susceptibility $\chi^{(3)}$ of the sample to provide contrast [5, 6, 7], and has proved effective for imaging biological samples [8, 9, 10, 11, 12, 13]. The imaging properties of THG microscopy strongly depend on the field distribution near focus. The most salient characteristic of THG microscopy with Gaussian beams is that no signal is obtained from a homogeneous normally dispersive sample [5]. Signal is obtained around $\chi^{(3)}$ inhomo-

#98503 - $15.00 USD Received 8 Jul 2008; revised 21 Aug 2008; accepted 21 Aug 2008; published 3 Sep 2008

geneities, with an efficiency depending on the relative sizes of the inhomogeneity and of the focal volume [14]. Since most materials have a non-negligible $\chi^{(3)}$, THG signal creation for a particular sample geometry is essentially determined by interference effects. Focus engineered THG microscopy is therefore expected to give access to sub-wavelength structural information about the sample. We here present a numerical study of vectorial and phase-matching aspects of THG by tightly focused Gaussian, Hermite-Gaussian (*HG*), and Laguerre-Gaussian (*LG*) beams incident on slabs, interfaces, and axially periodic samples. These calculations provide insight on the interplay between field and sample structure in THG microscopy with focused complex beams, and should more generally prove useful for designing coherent nonlinear microscopy (SHG, THG, CARS) experiments with engineered beams. Our strategy for simulations follows the framework described in [15], but integrates a complete vector field model to account for vectorial effects with arbitrary excitation beam profiles.

2. Theory and numerical implementation

A general method for analyzing signal generation in nonlinear microscopy can be described as follows (see Figure 1 for notations). First, the focal field distribution is calculated using a Debye-Wolf diffraction integral [16]. Then the induced nonlinear polarization in the focal volume is calculated for a given sample geometry. Finally, the resulting nonlinear field is propagated using Green's functions into the far field [15], where signal level and radiation patterns are analyzed. This theoretical description is summarized below.

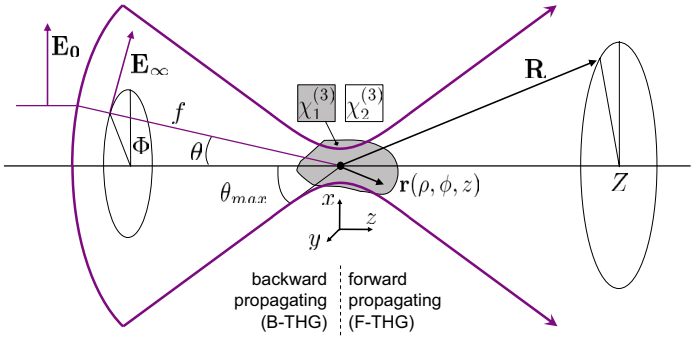

Fig. 1. Geometry and notations (see text)

2.1. *Excitation field near focus*

The field distribution near the focus of a high numerical aperture (NA) and anti-reflexion-coated objective lens given an arbitrary field at the back pupil can be calculated using the angular spectrum representation method [16, 17]:

$$\mathbf{E}(\rho,\phi,z) = \frac{ik_\omega f e^{-ik_\omega f}}{2\pi} \int_0^{\theta_m} \int_0^{2\pi} e^{-ik_\omega z cos(\theta)} e^{-ik\rho sin(\theta) cos(\Phi-\phi)} sin(\theta) \mathbf{E}_\infty(\theta,\Phi) d\Phi d\theta \quad (1)$$

with:

$$\mathbf{E}_\infty(\theta,\Phi) = (cos\,\theta)^{1/2} \left[\mathbf{E}_0(\theta,\Phi) \cdot \begin{pmatrix} -sin\,\Phi \\ cos\,\Phi \\ 0 \end{pmatrix} \right] \begin{pmatrix} -sin\,\Phi \\ cos\,\Phi \\ 0 \end{pmatrix}$$

#98503 - $15.00 USD Received 8 Jul 2008; revised 21 Aug 2008; accepted 21 Aug 2008; published 3 Sep 2008

$$+ \quad (cos\,\theta)^{1/2}\left[\mathbf{E}_0(\theta,\Phi)\cdot\begin{pmatrix} cos\,\Phi \\ sin\,\Phi \\ 0 \end{pmatrix}\right]\begin{pmatrix} cos\,\Phi\,cos\,\theta \\ sin\,\Phi\,cos\,\theta \\ -sin\,\theta \end{pmatrix} \tag{2}$$

where $\mathbf{E}_0(\theta,\Phi)$ describes the field phase and intensity distribution at the back aperture of the objective, $k = k_\omega = 2\pi\omega/n_\omega$ is the wavenumber, f is the focal length of the objective, n_ω is the refractive index at frequency ω, (ρ,θ,z) are cylindrical coordinates near focus, and $\theta_{max} = sin^{-1}(NA/n)$ is the maximum focusing angle of the objective.

If we expand $\mathbf{E}_0(\theta,\Phi)$ as a polynomial expansion of $cos(\Phi)$ and $sin(\Phi)$ functions, this 2D integral can be reduced to a 1D integral involving Bessel functions J_n. We can then use the following abbreviations to express the focal fields of the various beam modes considered in this study:

$$I_{lmn}^{\alpha\beta}(\rho,z) = \int_\alpha^\beta f_w(\theta)(cos\theta)^{1/2} sin^m\theta cos^n\theta J_l(k\rho sin\theta)e^{ikzcos\theta}d\theta \tag{3}$$

where $f_w(\theta) = exp(-(sin(\theta)/(f_0\,sin\theta_{max}))^2)$ is a filling factor that takes into account the ratio (f_0) between the beam size (related to w_0) and the back aperture of the objective ($f\,sin\theta_{max}$).

We introduce the following shorthand notations:

$$I_{lmn} = I_{lmn}^{0\theta_{max}} \;\; ; \;\; E_1 = \frac{ikf}{2}E_0e^{-ikf} \;\; ; \;\; E_2 = \frac{ikf^2}{2w_0}E_0e^{-ikf} \tag{4}$$

Expressions for focused Hermite-Gaussian and Laguerre-Gaussian modes can then be derived as [17] :

Focused $x-$ polarized HG_{00} (Gaussian) mode:

$$\mathbf{E}(\rho,\phi,z) = E_1\begin{bmatrix} I_{010}+I_{011}+(I_{210}-I_{211})cos(2\phi) \\ (I_{210}-I_{211})sin(2\phi) \\ -2iI_{120}cos\phi \end{bmatrix} \tag{5}$$

Focused $x-$ polarized HG_{10} mode:

$$\mathbf{E}(\rho,\phi,z) = E_2\begin{bmatrix} i(I_{120}+3I_{121})cos\phi + i(I_{320}-I_{321})cos(3\phi) \\ -i(I_{120}-I_{121})sin\phi + i(I_{320}-I_{321})sin(3\phi) \\ -2iI_{030}+2I_{230}cos(2\phi) \end{bmatrix} \tag{6}$$

Focused $x-$ polarized HG_{01} mode:

$$\mathbf{E}(\rho,\phi,z) = E_2\begin{bmatrix} i(3I_{120}+I_{121})sin\phi + i(I_{320}-I_{321})sin(3\phi) \\ -i(2I_{120}-2I_{121})cos\phi - i(I_{320}-I_{321})cos(3\phi) \\ 2I_{230}sin(2\phi) \end{bmatrix} \tag{7}$$

Focused $x-$ polarized HG_{20} mode:

$$\mathbf{E}(\rho,\phi,z) = E_2\begin{bmatrix} 3I_{031}-2(I_{010}+I_{011})-2cos(2\phi)[2I_{231}+I_{210}-I_{211}]+cos(4\phi)I_{140} \\ 2sin(2\phi)[I_{230}-I_{231}+I_{211}-I_{210}]+2sin(4\phi)[I_{431}-I_{430}] \\ cos(\phi)[4I_{120}-3I_{140}]+2icos(3\phi)I_{340} \end{bmatrix} \tag{8}$$

Focused linearly polarized LG_{01}^{lin} ('donut') mode:

$$LG_{01}^{lin} = HG_{10} + iHG_{01} \tag{9}$$

Focused azimuthally polarized LG_{01}^{az} mode:

#98503 - $15.00 USD Received 8 Jul 2008; revised 21 Aug 2008; accepted 21 Aug 2008; published 3 Sep 2008

$$\mathbf{E}(\rho,\phi,z) = E_2 \begin{bmatrix} 4iI_{120}sin\phi \\ -4iI_{120}cos\phi \\ 0 \end{bmatrix} \tag{10}$$

Focused radially polarized LG_{01}^{rad} mode:

$$\mathbf{E}(\rho,\phi,z) = E_2 \begin{bmatrix} 4iI_{121}cos\phi \\ 4iI_{121}sin\phi \\ -4I_{030} \end{bmatrix} \tag{11}$$

For future reference in this article, we summarize the calculated field distributions near focus for these various cases in Figure 2. Phase distributions are presented without the propagation term $exp(-ik_\omega z)$ in order to highlight the differences between the modes.

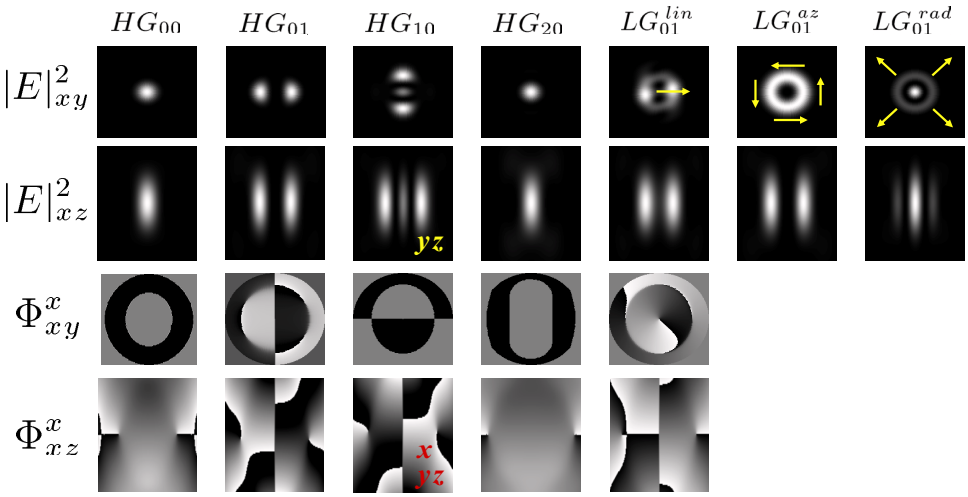

Fig. 2. Distributions in the *xy* and *xz* planes of the focal field intensity and of the phase of the *x*-polarized component when relevant, for the modes described by Eqs.(5-11). Arrows indicate the direction of polarization in the *xy* plane for focused LG_{01} beams. Intensity plots are normalized to their maximum values. Phase color table ranges from white ($-\pi$ rad) to black (π rad). $NA = 1.4,\ x,y \in [-1\ 1]\mu m,\ z \in [-2\ 2]\mu m$.

2.2. Calculation of the induced third-order non-linear polarization

In a medium characterized by its third-order nonlinear tensor $\chi^{(3)}_{ijkl}(\mathbf{r})$, the excitation field induces a polarization density described by:

$$P_i^{(3\omega)} = \sum_{j,k,l} \chi^{(3)}_{ijkl} E_j E_k E_l \tag{12}$$

The $\chi^{(3)}$ tensor of a homogeneous isotropic medium can be expressed as [18]:

$$\chi^{(3)}_{ijkl} = \chi_0(\delta_{ij}\delta_{kl} + \delta_{ik}\delta_{jl} + \delta_{il}\delta_{jk}) \tag{13}$$

We can then express the nonlinear polarization induced by the exciting field E in cartesian coordinates as:

$$\mathbf{P}^{(3\omega)} = \chi_0 \begin{bmatrix} E_x(3E_x^2 + E_y^2 + E_z^2) \\ E_y(E_x^2 + 3E_y^2 + E_z^2) \\ E_z(E_x^2 + E_y^2 + 3E_z^2) \end{bmatrix} \tag{14}$$

#98503 - $15.00 USD Received 8 Jul 2008; revised 21 Aug 2008; accepted 21 Aug 2008; published 3 Sep 2008

2.3. Propagation of the harmonic field

Finally, the harmonic field originating from all positions **r** in the focal region and propagated to a position **R** in the collection optics aperture can be expressed as [17, 15]:

$$E_{FF}(\mathbf{R}) = \int_V \mathbf{P}^{(3\omega)}(\mathbf{r})\mathbf{G}_{FF}(\mathbf{R}-\mathbf{r})dV \tag{15}$$

where V spans the excitation volume and $\mathbf{G}_{FF}$ is the far field Green's function:

$$\mathbf{G}_{FF} = \frac{exp(ikR)}{4\pi R}[\mathbf{I} - \mathbf{RR}/R^2] \tag{16}$$

where **R** is the coordinate of a point in the far field (see Fig. 1) and **I** is the third-order identity tensor.

Emission diagrams can be analyzed from these equations by calculating the squared harmonic field $|E_{FF}(\mathbf{R})|^2$ at different positions **R**. Alternatively, total THG power emitted in the forward (F-THG) or backward (B-THG) directions can be estimated by integrating $|E_{FF}(\mathbf{R})|^2$ over the front aperture of an epicollecting or trans-collecting objective.

To simplify the analysis of the results, we assume no linear index mismatch and we neglect temporal aspects such as group velocity mismatch for ultrashort pulses. However we assume that the samples consist of normally dispersive media (which is usually the case in biological THG imaging), since dispersion plays a significant role in THG contrast formation: for example, negative dispersion in homogeneous gas samples can result in bulk emission [18].

2.4. Numerical implementation

Calculations are performed using Matlab. We typically discretize the focal volume over a $200 \times 140 \times 140 \times (\lambda/40)$ grid, and evaluate the excitation field using quadrature algorithms. Unless otherwise stated, we use the following parameters: $\lambda = 1.2\mu m$, $NA = 1.4$ or 1.2, $f_0 = 2$, $n_\omega = 1.5$, $n_{3\omega} = 1.52$. We note that incorporating positive dispersion in the model is numerically advantageous because smaller focal volumes can be considered, and calculations are generally less noise-sensitive than in the limit case of zero-dispersion. For a given sample/focal field combination, we calculate the projection of the forward- and backward- emission patterns on planes perpendicular to the optical axis located at $Z = \pm 10cm$. We choose to present projected far-field patterns rather than angular emission diagrams because they appeared to be more readable in the case of complex emission profiles. For the interface and slab sample geometries, we assume that the focal volume encompasses two homogeneous isotropic media with third-order nonlinear susceptibilities $\chi_1^{(3)} = 1$ and $\chi_2^{(3)} = 0$. This choice is motivated by the fact that, for excitation geometries where bulk THG emission is canceled by destructive interference, THG from an interface scales as $|\chi_1^{(3)} - \chi_2^{(3)}|^2$. For periodic samples, we assume a sine-like variation $\chi^{(3)} = 1 + sin(2\pi z/\delta e)/2$ along the optical axis. We then iterate for each beam shape and for various sample positions the calculation of emission patterns, F-THG and B-THG powers. Normalization is done by considering the same total intensity in the focal volume for every mode.

3. Results

3.1. Vectorial aspect of THG microscopy with tightly focused beams

Although studies of THG by focused Gaussian beams generally neglect vectorial aspects, a general analysis of THG microscopy requires *a priori* a vector field model because high NA focusing does not preserve linear polarization. Furthermore it is seen from Eq.14 that the induced

#98503 - $15.00 USD Received 8 Jul 2008; revised 21 Aug 2008; accepted 21 Aug 2008; published 3 Sep 2008

nonlinear polarization $\mathbf{P}^{(3\omega)}$ can *linearly* depend on a particular field component. For example if E_z is strong at a particular location near focus and spatially overlaps with E_x, a cross-term proportional to $E_z E_x^2$ will significantly contribute to $\mathbf{P}_x^{(3\omega)}$. Conversely if E_z does not overlap with E_x, only the E_x^3 term will contribute to the TH signal. In particular, in the case of a tightly focused Gaussian beam with initial linear polarization the axial component near focus is important (see Fig. 3): $Max(E_z) \approx Max(E_x)/3$ for $NA = 1.4$. However in this case there is little overlap between E_x and E_z, so that E_z contributes little to THG. Thus, a scalar approximation will usually work well for THG from simple interfaces excited by a focused linearly polarized Gaussian beam. However it will typically not be accurate for higher-order beam shapes or other input polarization patterns. Recalling that the phase distribution (including the Gouy shift) is generally different for the various field components [17, 19], cross-terms may define different coherence lengths within the focal volume and affect the imaging properties. Furthermore, focused radially polarized beams typically exhibit strong axial components (see e.g. LG_{01}^{rad} mode in Fig. 3) [20, 1, 2] which give them original imaging properties.

We also point out that a well-described vectorial aspect of THG microscopy is the absence of THG signal when a HG_{00} beam with circular polarization is focused on an interface between isotropic media [9].

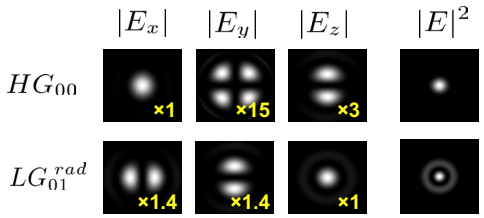

Fig. 3. Distribution of the different field polarization components and total intensity in the transverse focal plane for focused HG_{00} and LG_{01}^{rad} beams. $x,y \in [-1\ 1]\mu m$.

3.2. THG imaging of XY interfaces with HG and LG beams

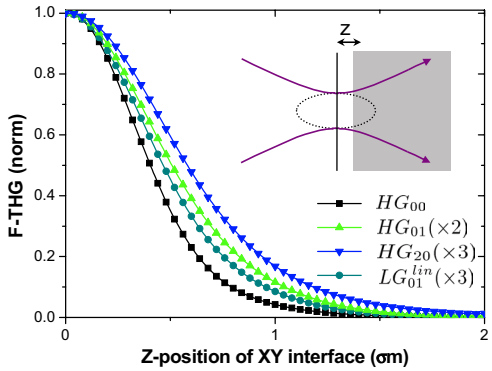

Fig. 4. F-THG during an axial scan through a xy interface with HG and LG beams. Curves are normalized by the factors indicated in the inset.

We begin our study of THG microscopy with non-standard beams by considering the simplest sample geometry, namely an interface between two media with different nonlinear susceptibil-

#98503 - $15.00 USD Received 8 Jul 2008; revised 21 Aug 2008; accepted 21 Aug 2008; published 3 Sep 2008

ities $\chi_1^{(3)}$ and $\chi_2^{(3)}$. A well-known fact in the case of a XY-interface (i.e. perpendicular to the optical axis) excited by a tightly focused HG_{00} beam is that a z-scan produces a symmetric Gaussian (or Lorentzian if the objective aperture is overfilled) curve peaking when the interface is at the focus. Our simulations predict similar behaviors for THG emission with all the higher-order HG and LG modes considered in this study (see Fig. 4 for characteristic examples), whether or not they possess cylindrical symmetry. The main difference lies in the widths of the z-scan responses, which are related to the axial extents of the corresponding excitation field distributions. The single-peaked nature of the z-scans reflects the fact that the modes considered here exhibit a single axial maximum. We note that emission is essentially forward-directed, as in the case of Gaussian excitation [21]. However different modes produce different emission patterns. For example, on-axis harmonic emission is prevented with focused HG_{01} modes due to the laterally antisymmetric nature of the focal phase distribution, as predicted for CARS emission from bulk media [3].

We also point out that the HG_{00} case is qualitatively well-described by the paraxial approximation (not shown) even at high NA (in contrast with [15] where an inappropriate value of the confocal parameter was used). Paraxial approximation provides meaningful results for nonlinear processes involving Gaussian beams and simple geometries because over the region of highest intensity where most signal creation occurs, both the intensity and the Gouy phase shift (which varies almost linearly with z) are accurately approximated. Of course, the situation can be quite different with complex field distributions.

3.3. THG imaging of XZ/YZ interfaces with focused HG beams

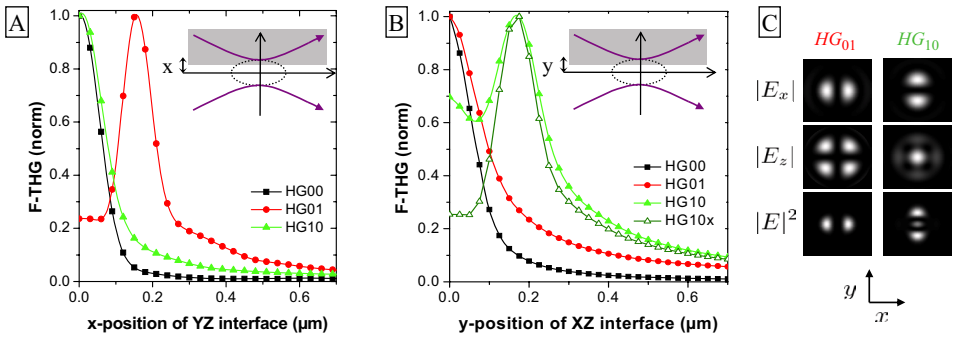

Fig. 5. F-THG during lateral scans through interfaces parallel to the optical axis. (a) $x-$scan through a YZ interface. (b) $y-$scan through a XZ interface. The HG_{10x} curve (empty green triangles) is the behavior predicted when the z component of HG_{10} is omitted. (c) Excitation field and intensity distribution in the focal plane for focused HG_{01} and HG_{10} beams.

More interesting is the case of an interface parallel to the optical axis excited by an asymmetric field distribution such as a focused HG_{01} or HG_{10} beam. When a YZ interface is $x-$scanned across a focused HG_{01} beam (Fig. 5(a)), the F-THG response exhibits a double peak reflecting the field distribution in the focal plane (see Fig. 5(c)), contrasting with the case of a focused HG_{00} or HG_{10}. Even more striking is the case of a XZ interface being $y-$scanned across a focused HG_{10} beam (Fig. 5(b)). In this case the THG response exhibits a triple peak. The central peak results from the presence of a significant axially polarized component in the strongly focused x-polarized HG_{10} field (I_{030} term in Eq. 6 which is not present in the HG_{01} case, see also Fig. 5(c)). This vectorial interpretation is corroborated by the double-peaked shape of the THG $y-$scan obtained when the axial component is omitted in the simulation (Fig. 5(b)).

#98503 - $15.00 USD Received 8 Jul 2008; revised 21 Aug 2008; accepted 21 Aug 2008; published 3 Sep 2008

Since this situation is equivalent to that of a single half-space with susceptibility $|\chi_1^{(3)} - \chi_2^{(3)}|$, maximum emission is obtained when one of the two main excitation peaks is incident on the interface.

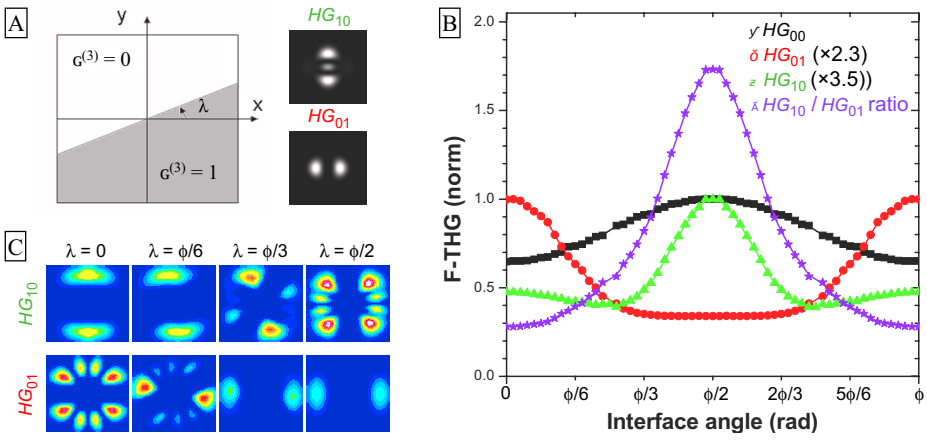

Fig. 6. Sensitivity to the orientation of an interface parallel to the optical axis using asymmetric excitation (HG_{01} and HG_{10}). (a) Geometry of the sample and distribution of the excitation intensity in the focal plane. (b) Normalized F-THG signal as a function of interface angle ϕ for HG_{00} (black squares), HG_{01} (red discs) and HG_{10} (green triangles). Normalization factors are indicated in the inset. The HG_{10}/HG_{01} signal ratio (purple stars) probes the interface orientation within the focal volume with good contrast. (c) Projected far-field emission patterns as a function of interface angle for HG_{01} and HG_{10} excitation. (Media1): TH emission patterns for HG_{00}, HG_{01}, and HG_{10} excitation, as a function of interface orientation. Patterns are evaluated at z=+10cm over a 15×15cm area transverse to the optical axis, which corresponds to a detection NA of approximately 0.5.

We now seek to take advantage of the laterally asymmetric nature of odd HG beams to probe sample orientation. We analyze the THG response obtained from HG_{01} and HG_{10} beams focused on an interface parallel to the optical axis as a function of the angle ϕ that it makes relative to the X axis (see Fig. 6(a)). As anticipated from the shape of the focal fields, THG emission is strongly modulated (>50%) as a function of the interface angle. This is because the geometry is roughly equivalent to that of a single-peaked excitation where the distance between the focal spot and the interface is proportional to the sine (or cosine) of the interface angle. Therefore, anti-correlated behaviors are predicted with HG_{01} and HG_{10} beams (Fig. 6(b)), and a combination of measurements with two such beam shapes provides sub-μm information about sample orientation. The corresponding far-field emission patterns exhibit even more subtle variations (Fig. 6(c)). When the two main peaks of the focal field lie on both sides of the interface (i.e. $\phi = 0$ with HG_{10} excitation or $\phi = 90$ with HG_{01} excitation), F-THG emission occurs along two off-axis lobes. These emission patterns are reminiscent of the case of Gaussian excitation of a XY interface [15], where the Gouy shift prevents on-axis phase matching and deflects the emission. However when both excitation peaks are incident on the interface (i.e. $\phi \approx 90$ with HG_{01} or $\phi \approx 0$ with HG_{10}), the emission originates from two sources and interferences structure it into a non-trivial 8-lobes pattern. The relative intensities of these lobes are tightly related to the sample orientation (Fig. 6). See (Media1).

#98503 - $15.00 USD Received 8 Jul 2008; revised 21 Aug 2008; accepted 21 Aug 2008; published 3 Sep 2008

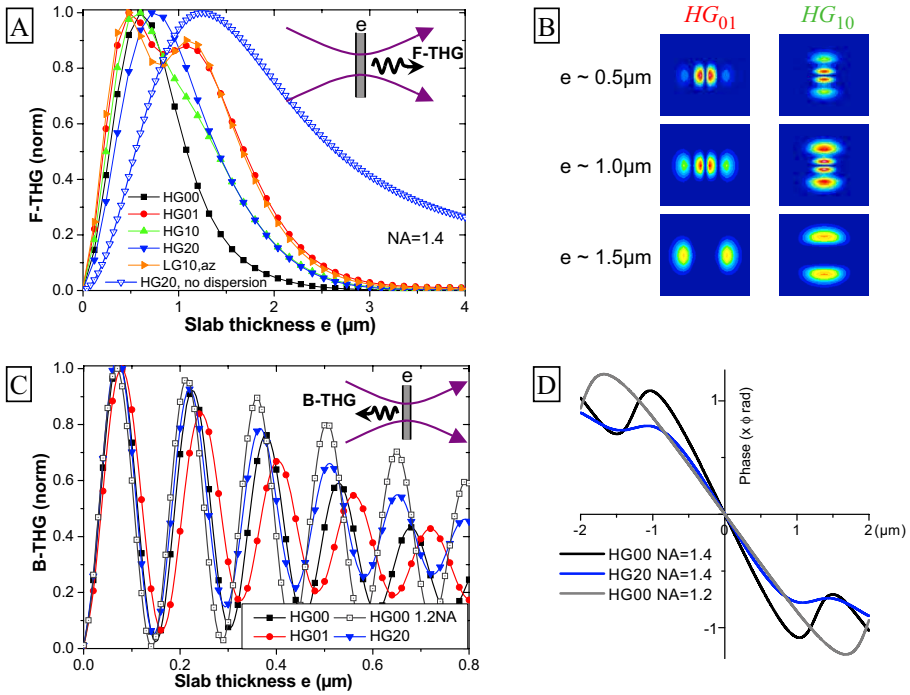

Fig. 7. F-THG and B-THG from slabs of varying thicknesses using different beam shapes. (a) F-THG as a function of slab thickness indicates the forward coherence length associated with a particular field profile. The inset depicts the corresponding geometry. HG_{20} excitation (blue triangles) results in larger forward coherence length than HG_{00} (black squares). HG_{01} excitation (red disc) produce a double-peaked response as a function of thickness, corresponding to distinct emission patterns. The double peak behavior is blurred for HG_{10} excitation (see text). The HG_{20} case without dispersion is also presented for comparison (empty triangles). For all the modes considered here, the peak TH signal intensity is between 1.5 and 2 times higher than that obtained from a semi-infinite slab. (b) Far-field emission patterns using HG_{01} and HG_{10} excitation, for different slab thicknesses. (c) B-THG as a function of slab thickness, according to the geometry depicted in the inset. Oscillation period indicates the backward coherence length. (d) On-axis phase distribution (without propagation term) for HG_{00} and HG_{20} modes with different NAs.

#98503 - $15.00 USD Received 8 Jul 2008; revised 21 Aug 2008; accepted 21 Aug 2008; published 3 Sep 2008

3.4. Focus-engineered THG from slabs

Coherent nonlinear microscopies are particularly sensitive to the axial phase distribution in the regions of highest intensity. In THG microscopy with HG_{00} excitation, the Gouy shift defines a signal coherent construction length of $\approx 0.7\lambda$ for forward emission (F-THG) [15] and the wave vector mismatch Δk defines a construction length of $\pi/\Delta k \approx \lambda/12n_\omega$ for backward emission (B-THG) [21]. The coherence length for forward emission has a major influence on imaging properties, since it acts as a spatial bandpass filter that highlights objects of a given size in F-THG images [14]. Elaborating on this idea, we point out that when focusing non-Gaussian beams such as higher-order *HG* and *LG* modes, focal field components exhibit altered phase distributions [19, 22] (see e.g. Fig. 7(d)).

We therefore simulate F-THG and B-THG from slabs of varying thicknesses to gain insight into the axial coherence lengths associated with non-Gaussian beams. Fig. 7 shows that forward- and backward- coherence lengths can indeed be modulated when using alternate modes. A particularly clear illustration comes when comparing HG_{00} and HG_{20} excitations. Focused HG_{20} resembles HG_{00} because it exhibits a single peak along the optical axis, albeit with a slower phase variation and a broader intensity distribution than focused HG_{00}. Accordingly, the axial coherence length is increased for F-THG and reduced for B-THG. Reduced B-THG coherence length manifests itself through the reduced oscillation period as a function of slab thickness (Fig. 7(c)). We point out that moving from HG_{00} to HG_{20} excitation here produces an effect comparable to changing the excitation NA from 1.4 to ≈ 1.2 (see Fig. 7(d)) and comes at the cost of reduced signal level by a factor ≈ 2. Fig. 7(a) also illustrates the consequence of including/excluding dispersion, for the HG20 case (filled and empty blue triangles). For all the cases studied here, we essentially find that dispersion reduces TH efficiency for large objects without affecting the relative behaviors obtained with different beam shapes.

However beam shaping offers more degrees of freedom than merely changing the NA. This is exemplified by the dependence on slab thickness of F-THG with e.g. HG_{01} excitation. The thickness response is double-peaked, and can be seen as resulting from two different coherence lengths with the two components exhibiting distinct emission patterns (see Fig. 7(b)). This behavior is related to the dominating I_{120} terms in Eq. 7, and is not obtained with HG_{10} excitation because the *z*-polarized I_{030} term (Eq. 6) produces an additional contribution that blurs the double-peak behavior. Even more dramatic effects can be obtained when imaging complex samples, as will be discussed in the next section.

3.5. Focus-engineered THG from axially periodic structures

THG emission from dielectric media excited with Gaussian beams is mostly forward-directed [21] and vanishes in a homogeneous medium. The forward-directed nature of the emission stems from the fact that the large wave vector mismatch in the backward direction Δk limits signal creation to a small region ($\approx 65nm$ for $\lambda = 1200nm$ and $n_\omega = 1.5$) around an heterogeneity (see fig 7). However the situation can be quite different in the case of a structured sample: if the sample exhibits appropriate axial periodicity, the density distribution of emitters can provide an additional momentum that puts the emitted waves in phase in a particular direction [21, 23]. Efficient THG emission may be obtained either in the forward or backward direction, depending on sample structure. Under HG_{00} excitation focused at 1.4 NA, an axial sine-like $\chi^{(3)}$ modulation with spatial period $\delta e \approx 2\pi/\Delta k \approx \lambda/6n_\omega = 135nm$ is expected to produce efficient B-THG emission, and a similar distribution with $\delta e \approx 2\mu m$ is expected to produce efficient F-THG emission [21].

This idea can be pushed further with focal field engineering: alternative field distributions can modify these spatial resonances. Figure 8 presents the dependence of B-THG and F-THG on sample spatial period, for the set of beam modes considered in this study. Resonances are

#98503 - $15.00 USD Received 8 Jul 2008; revised 21 Aug 2008; accepted 21 Aug 2008; published 3 Sep 2008

observed for both F-THG and B-THG for all excitation modes, with pronounced differences depending on the focal field profile. We note that although the precise axial localization of the sample can modulate the THG power by up to 40%, it does not significantly change the resonances (not shown). Not surprisingly, the characteristic sample lengths that enhance F-THG emission using HG modes are reminiscent of the coherence lengths that can be estimated by F-THG from slabs (Fig. 8). The backward emission behaviors are more complex, particularly for polarization-shaped LG_{01} beams. Together, these calculations show that the measurement of F-THG and B-THG with a properly chosen set of beam shapes can provide information on sample characteristic lengths in the ranges $130-250nm$ and $0.7-7\mu m$. We point out that the angular emission patterns are also closely related to the sample spatial frequencies (Fig. 8). Finally we note that these ideas are transposable to other coherent processes such as SHG and CARS. For example, efficient backward emission with HG_{00} excitation should be possible from a structure exhibiting a spatial frequency of $\delta e \approx \lambda/4n_\omega$ for SHG and $\delta e \approx \lambda_{as}/2n_{as}$ (where *as* refer to the anti-Stokes frequency) for CARS. Excitation with alternative field distributions is expected to shift these spatial resonances.

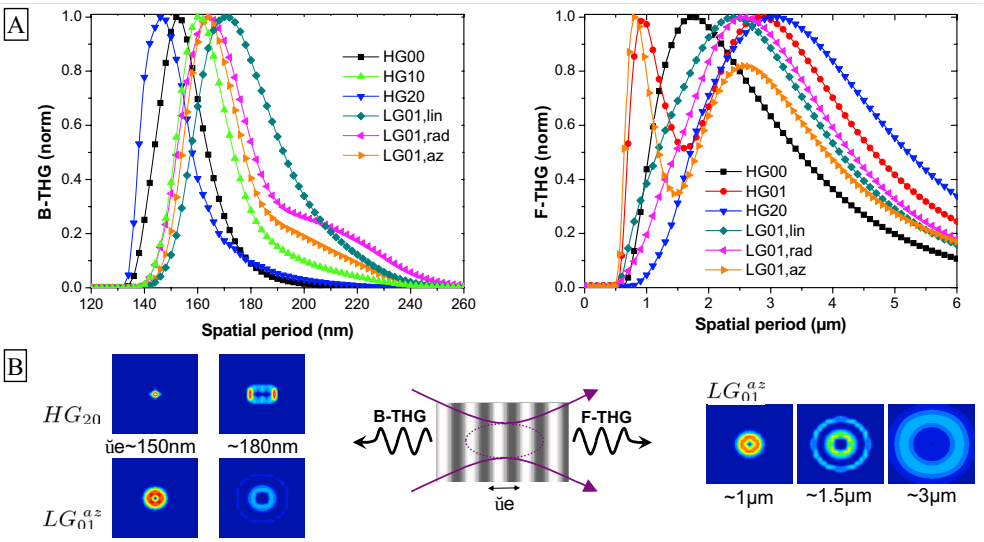

Fig. 8. F-THG and B-THG signal obtained from an axially periodic sample using different focal field distributions. (a) B-THG and F-THG as a function of sample period, for various *HG* and polarization-shaped LG_{01} beams. Different field shapes result in different spatial resonances. THG measurements with a properly chosen set of beam shapes provide information on sample characteristic lengths at different scales. Normalization factors for B-THG (resp F-THG) curves with respect to F-THG from a semi-infinite slab with a gaussian excitation: $HG_{00}\times 1.5(\times 2)$; $HG_{01}\times 1(\times 1)$; $HG_{10}\times 0.4(\times 0.3)$; $HG_{20}\times 0.3(\times 0.3)$; $LG_{01}^{lin}\times 0.3(\times 0.4)$; $LG_{01}^{rad}\times 0.1(\times 0.1)$; $LG_{01}^{az}\times 0.5(\times 0.6)$. (b) Characteristic examples of emission patterns in the forward and backward direction, as a function of sample periodicity.

4. Conclusion

Focal field engineering for coherent nonlinear microscopy is a rich and promising subject. The general idea is that measurable emission patterns reflect the interplay between the (unknown) sample structure and a known field distribution. The vectorial and phase properties of tightly

#98503 - $15.00 USD Received 8 Jul 2008; revised 21 Aug 2008; accepted 21 Aug 2008; published 3 Sep 2008

focused higher-order beams are an active area of research [24, 25, 22], and so are the vectorial aspects of nonlinear microscopy [2, 26]. Studying focus-engineered THG is informative because third-harmonic generation can be obtained from simple (isotropic) sample geometries and is highly sensitive to the focal phase distribution. Therefore it is a convenient means to study the impact of focus engineering on phase-matching conditions. Moreover, THG microscopy is usually a non-spectroscopic, structure-sensitive [14] imaging technique that provides morphological information about unstained samples. The results presented here show the potential of focus-engineered THG microscopy to provide sub-resolution information about complex samples: angles and characteristic lengths in the $130-250nm$ range are reflected in the emission patterns and can be probed using simple ratiometric measurements. A perspective is to design pupil functions producing a targeted field distribution [27, 28], axial field engineering (bottle beams [3], etc) being of particular relevance. Finally we note that the ideas explored in this article are generally transposable to other imaging modalities such as CARS and SHG. For example, CARS emission from an axial interface excited with a laterally asymmetric field distributions should exhibit a behavior similar that shown in Fig. 6(b). Also, focus engineering can be used to alter the spatial resonances resulting in efficient SHG and CARS emission in a particular direction, as in Fig. 8. It is anticipated that additional studies will explore the potential of focal field engineering for coherent nonlinear microscopy.

Acknowledgments

We thank Marie-Claire Schanne-Klein, François Hache and Paul Abbyad for comments on the manuscript, and Daniel Côté for seminal discussions. This work was supported by the Délégation Générale pour l'Armement (DGA) and by the Agence Nationale de la Recherche (ANR).

#98503 - $15.00 USD Received 8 Jul 2008; revised 21 Aug 2008; accepted 21 Aug 2008; published 3 Sep 2008